

Laminar, Transitional, and Turbulent Heating on Mid Lift-to-Drag Ratio Entry Vehicles

Brian R. Hollis*

NASA Langley Research Center, Hampton, Virginia 23681

and

Kevin E. Hollingsworth†

Aerospace Computing, Inc., Hampton, Virginia 23681

DOI: 10.2514/1.A32458

The boundary-layer transition characteristics and convective aeroheating levels on mid lift-to-drag ratio entry vehicle configurations have been studied through wind-tunnel testing. Several configurations were investigated, including elliptically blunted cylinders with both circular and elliptically flattened cross sections, biconic geometries based on launch vehicle dual-use shrouds, and parametrically optimized analytic geometries. Vehicles of this class have been proposed for high-mass Mars missions, such as sample return and crewed exploration, for which the conventional sphere-cone entry-vehicle geometries of previous Mars missions are insufficient. Testing was conducted at Mach 6 over a range of Reynolds numbers sufficient to generate laminar, transitional, and turbulent flow. Transition onset locations, both straight-line and cross-flow, and heating rates were obtained through global phosphor thermography. Supporting computations were performed to obtain heating rates for comparison with the data. Laminar data and predictions agreed to well within the experimental uncertainty. Fully turbulent data and predictions also agreed well. However, in transitional flow regions, greater differences were observed.

Nomenclature

a_{lower}	= vehicle geometric parameter for ellipsled cross-section major axis, in.
a_{nose}	= vehicle geometric parameter for ellipsled nose major axis, in.
b_{lower}	= vehicle geometric parameter for ellipsled cross-section minor axis, in.
b_{nose}	= vehicle geometric parameter for ellipsled nose minor axis, in.
C_D	= drag coefficient
C_p	= local surface pressure coefficient
$C_{p,\text{max}}$	= maximum surface pressure coefficient
D	= model or flight vehicle maximum diameter, in. or m
h	= heat-transfer film coefficient, kg/m/s ²
h_{FR}	= heat-transfer film coefficient based on Fay–Riddell theory, kg/m/s ²
H_w	= surface enthalpy, J/kg
H_0	= tunnel total enthalpy, J/kg
$H_{300\text{ K}}$	= enthalpy at 300 K, J/kg
L	= model or flight vehicle length, in. or m
L_1, L_2	= lengths for Hammerhead model first and second cone segments
L/D	= vehicle lift-to-drag ratio
M_∞	= freestream Mach number
m	= vehicle mass, kg
P_∞	= freestream pressure, Pa
q	= heat-transfer rate, W/cm ²
q_{FR}	= heat-transfer rate based on Fay–Riddell theory, W/cm ²
r_{nose}	= Hammerhead model nose radius, in.

r_{upper}	= model geometric parameter for ellipsled geometry cross section, in.
Re_∞	= freestream Reynolds number, 1/m or 1/ft
S	= reference area for aerodynamics, m ²
St	= Stanton number heat-transfer coefficient
T_∞	= freestream temperature, K
U_∞	= freestream velocity, m/s
x, y, z	= Cartesian coordinates, in. or m
α	= angle of attack, deg
β	= ballistic coefficient, kg/m ²
γ	= specific heat ratio
θ	= angle between geometry local surface normal and velocity vector
θ_1, θ_2	= angles for Hammerhead geometry first and second cones segments
μ_∞	= freestream viscosity, kg/m/s
ρ_∞	= freestream density, kg/m ³

I. Introduction

THE long-term goals of NASA's Mars exploration program include both robotic sample return missions and long-duration crewed missions. Such missions will require safe and precise landing of much larger masses than any previous Mars missions (10 to 50 mt). Recent systems analysis studies [1–4] have demonstrated that the heritage 70 deg sphere-cone entry vehicle architecture employed by every NASA mission to Mars, from Viking to Mars Science Laboratory (MSL), does not provide sufficient aerodynamic performance to decelerate and precisely target the desired landing site in the thin atmosphere of Mars. One of the architectures identified by these studies that would enable such missions is a mid lift-to-drag ratio (mid- L/D) (approximately 0.4 to 0.8) entry-vehicle geometry. Mid- L/D geometries have also been identified as candidates for outer planet missions (e.g., Neptune) for which aerocapture will be employed [5].

To ensure the success of a mission in which a mid- L/D geometry is employed, the aerodynamic and aerothermodynamic (both convective heating and shock-layer radiation) environments must be understood. Because mid- L/D geometries do not have the test, evaluation, and flight heritage of sphere-cone geometry entry vehicles, the current study was conducted to obtain experimental information on the convective aeroheating environment with a focus on boundary-layer transition behavior and turbulent heating levels.

Presented as Paper 2012-3063 at the 42nd AIAA Fluid Dynamics Conference and Exhibit, New Orleans, LA, 25–28 June 2012; received 13 July 2012; revision received 30 July 2012; accepted for publication 17 October 2012; published online 4 June 2013. This material is declared a work of the U.S. Government and is not subject to copyright protection in the United States. Copies of this paper may be made for personal or internal use, on condition that the copier pay the \$10.00 per-copy fee to the Copyright Clearance Center, Inc., 222 Rosewood Drive, Danvers, MA 01923; include the code 1533-6794/13 and \$10.00 in correspondence with the CCC.

*Aerospace Engineer, Aerothermodynamics Branch, Associate Fellow AIAA.

†Principal Engineer, Supersonic/Hypersonic Test Branch.

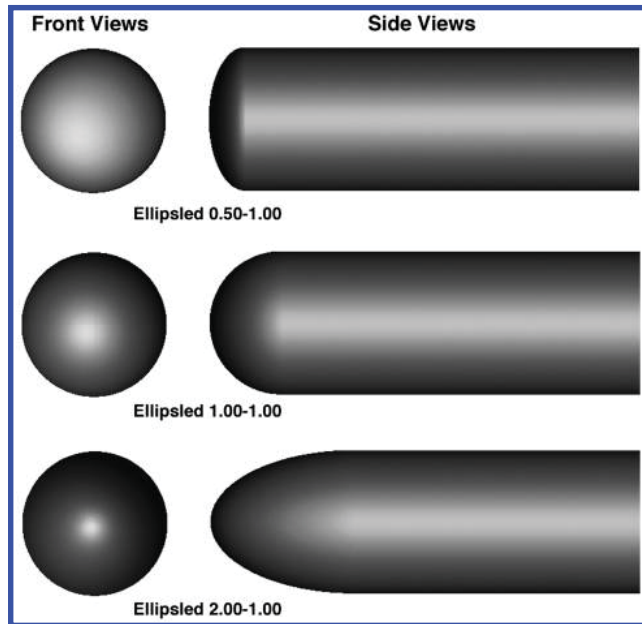


Fig. 1 Axisymmetric ellipsled geometries.

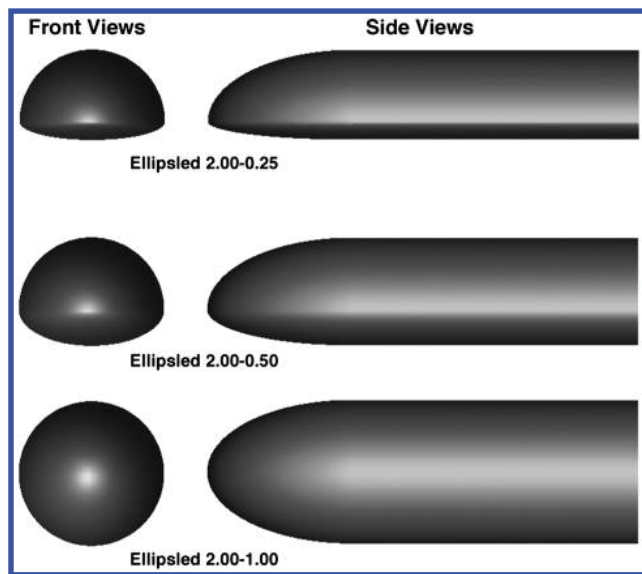


Fig. 2 Flattened ellipsled geometries.

An engineering-level analysis was also conducted to provide aerodynamic performance comparisons between the geometries.

II. Mid- L/D Geometries

Various geometries have been proposed and studied to meet the mid- L/D entry vehicle requirements depending on the mission in question. In the present study, three separate classes of geometries were studied to generate a parametric database on convective heating and boundary-layer transition that will be applicable to future design studies. The common thread between all geometries was the specification of a 30 m flight vehicle length, with a length-to-maximum diameter ratio of 3:1, which was the baseline defined in [1–4]. For wind-tunnel testing, a scale factor of 0.01016 was applied to produce 0.3048-m-long (12-in.-long) models. Also, the wind-tunnel models were fabricated with a narrow flat on the top (leeside) surface to aid in model positioning and alignment. In no way did this change from the nominal geometries affect the data on the bottom (wind-side) of the models.

A. Ellipsled Geometries

Ellipsled geometries, which consist of an elliptically blunted nose and a cylindrical aftbody, have been proposed for various exploration missions that require aerocapture [5,6]. Two subclasses of ellipsleds were considered herein: axisymmetric and flattened. The axisymmetric ellipsled has a circular cross section and the flattened ellipsled cross section is split between a circular top half and an elliptical bottom half. Five ellipsled geometries were tested. For the axisymmetric geometries, the ellipticity of the nose was varied in the longitudinal direction to create different nose bluntness factors, whereas for the flattened ellipsleds the cross-sectional ellipticity of the lower half of the geometry was varied to produce a flatter bottom. These geometries are shown in Figs. 1 and 2. The geometric parameters are defined in Fig. 3 and listed in Table 1. The naming convention employed is “Ellipsled xxx - yyy ”, where xxx represents the nose axes ratio $a_{\text{nose}}/b_{\text{nose}}$ and yyy represents the lower-body cross-section axes ratio $a_{\text{lower}}/b_{\text{lower}}$. Note that axisymmetric Ellipsled 2.00-1.00 is shown twice because it also represents the nominal case $a_{\text{lower}}/b_{\text{lower}} = 1$ of the flattened Ellipsled family.

B. Cooptimization of Blunt-Body Reentry Analysis Optimized Geometries

The cooptimization of blunt-body reentry analysis (COBRA) geometries were taken from [7], in which an optimization algorithm was developed to meet certain mission performance criteria; for example, landed mass, convective heating rate, aerodynamic performance, etc. Starting from a spherically capped cylinder (equivalent to the Ellipsled 1.00-1.00 geometry), a family of optimized geometries was generated that met the criteria for a high-mass Mars entry mission. Three representative geometries, COBRA-8459B, COBRA-14297B, and COBRA-14888B, were selected from this family for

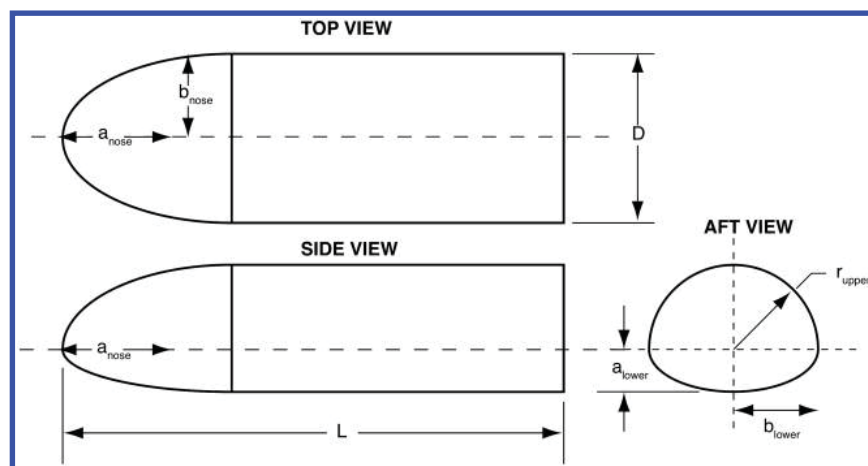


Fig. 3 Ellipsled geometry definition.

Table 1 Ellipsled geometry parameters

Geometry	L , in.	D , in.	a_{nose} , in.	b_{nose} , in.	$a_{\text{nose}}/b_{\text{nose}}$	r_{upper} , in.	a_{lower} , in.	b_{lower} , in.	$a_{\text{lower}}/b_{\text{lower}}$
Ellipsled 0.50-1.00	12.00	4.00	1.00	2.00	0.50	2.00	2.00	2.00	1.00
Ellipsled 1.00-1.00	12.00	4.00	2.00	2.00	1.00	2.00	2.00	2.00	1.00
Ellipsled 2.00-1.00	12.00	4.00	4.00	2.00	2.00	2.00	2.00	2.00	1.00
Ellipsled 2.00-0.25	12.00	4.00	4.00	2.00	2.00	2.00	0.50	2.00	0.25
Ellipsled 2.00-0.50	12.00	4.00	4.00	2.00	2.00	2.00	1.00	2.00	0.50

testing. These geometries are shown in Fig. 4. Additional information on these geometries is provided in [7].

C. Dual-Use Hammerhead Biconic Shroud Geometries

The biconic shroud family is based on a proposed dual-use Hammerhead shroud geometry for the Ares V heavy lifter [8,9]. Although the Ares V program has been cancelled, the general concept is applicable to any launch vehicle shroud. The shroud would be used during both ascent from Earth and entry/aerocapture at the destination. Three parametric geometries were developed for testing based on the Hammerhead biconic concept. Nose radius was the primary geometric variation, with the length of the first cone and angle of the second cone then being varied to fit the geometric constraints of a constant first-cone angle and constant second-cone

length. The rationale for these constraints was to minimize changes to the internal volume of the vehicle, which is a function mainly of the geometry of the second cone and cylindrical third section. These geometries are shown in Fig. 5 and the geometric parameters are defined in Fig. 6 and listed in Table 2.

III. Comparison of Aerodynamic Performance

To obtain a first-order understanding of the aerodynamics of the various configurations, a modified Newtonian analysis was performed. According to modified Newtonian theory, the aerodynamics of a vehicle travelling at hypersonic speed can be approximated by integration of the pressure coefficient C_p over the surface of the vehicle, where C_p is defined as

$$C_p = C_{p,\max} \cos^2 \theta \quad (1)$$

The maximum pressure coefficient $C_{p,\max}$ is the value obtained for a given freestream Mach number and specific heat ratio (for this case, $M_\infty = 30$ and $\gamma = 1.25$ were assumed) using the perfect-gas, normal shock relations. Theta θ is the angle between the local surface normal at a point on the body and the freestream velocity vector. For computations of force and moment coefficients from the C_p distributions, reference dimensions of $L = 30$ m and $S = 78.54$ m² (based on the area of a circular 10-m-diam base) were used for all geometries.

The figures of merit for the aerodynamic analysis were the lift-to-drag ratio (L/D) and the reduced (massless) ballistic coefficient β/m where

$$\beta = \frac{m}{C_D S} \quad (2)$$

The optimum aerodynamic performance is obtained for the highest L/D (for maneuverability and precision landing) at the lowest β (for greatest vehicle payload). These figures of merit are displayed in terms of L/D vs angle of attack (AOA) and L/D vs reduced ballistic coefficient in Figs. 7 and 8 for the ellipsled geometries, Figs. 9 and 10 for the COBRA geometries, and Figs. 11 and 12 for the Hammerhead geometries. The range of interest for mid- L/D performance (approximately 0.4 to 0.8) is highlighted in the figures. In addition, for each geometry, the AOA and reduced ballistic coefficient are tabulated for L/D (Table 3). In terms of these parameters, the flattened Ellipsled 2.00-0.25 produces the best performance and the axisymmetric Ellipsled 0.50-1.00 produces the worst performance. All geometries can meet the required L/D range within angles of attack of 30 to 70 deg except the Ellipsled 0.50-1.00 and Ellipsled

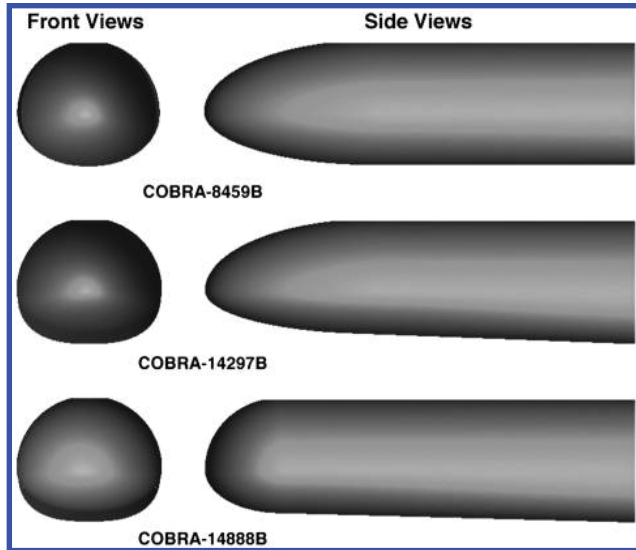


Fig. 4 COBRA geometries.

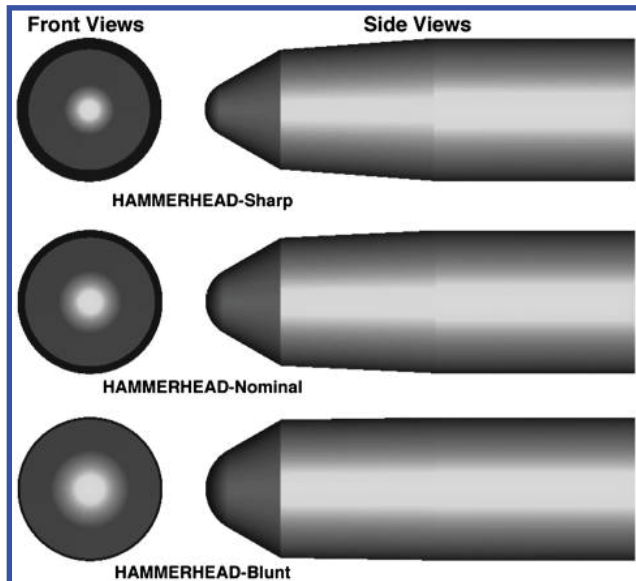


Fig. 5 Hammerhead biconic geometries.

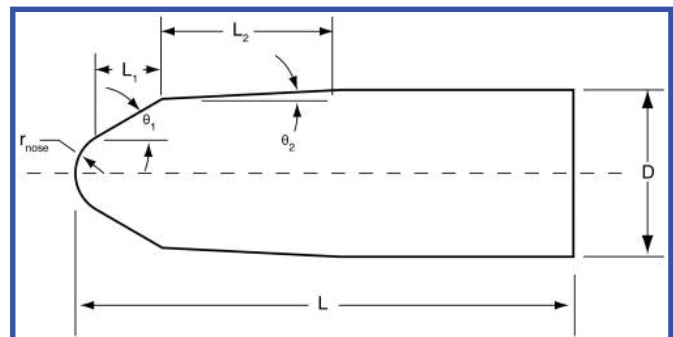


Fig. 6 Hammerhead geometry dimensions.

Table 2 Hammerhead geometry parameters

Geometry	L , in.	D , in.	r_{nose} , in.	θ_1 , deg	L_1 , in.	θ_2 , deg	L_2 , in.
Hammerhead-sharp	12.000	4.000	0.8000	30.0000	1.7000	4.3333	4.2981
Hammerhead-nominal	12.000	4.000	1.0000	30.0000	1.6000	2.8000	4.2981
Hammerhead-blunt	12.000	4.000	1.2500	30.0000	1.4750	0.8781	4.2981

1.00-1.00. However, in a complete mission system analysis, other constraints would also be considered, such as convective and shock-layer radiative heating; aerodynamic stability; internal payload layout and packaging; vehicle structural strength and manufacturability, etc.

IV. Facility and Test Technique

A. Description of NASA Langley Research Center 20 In. Mach 6 Air Tunnel

The NASA Langley Research Center 20 In. Mach 6 Air Tunnel (Fig. 13) is a blow-down facility in which heated, dried, and filtered air is used as the test gas. A detailed description of this facility can be found in [10]. The tunnel has a two-dimensional contoured nozzle that opens into a 20.5×20.0 in. (0.52×0.508 m) test section. The tunnel is equipped with a bottom-mounted injection system that can transfer a model from the sheltered model box to the tunnel centerline

in less than 0.5 s. Run times of up to 15 min are possible in this facility, although for the current aeroheating study, run times of only a few seconds were required. The nominal reservoir conditions of this facility produce perfect-gas freestream flows with Mach numbers between 5.8 and 6.1 and unit Reynolds numbers of 0.5×10^6 to $8.3 \times 10^6/\text{ft}$ (1.64×10^6 to $27.2 \times 10^6/\text{m}$). Conditions for the current test series are listed in Table 4. The heat-transfer values listed in this table are based on Fay–Riddell calculations for a reference 2 in. radius hemisphere at cold-wall (300 K) conditions. Five different Reynolds number points were employed with the intent of generating a range of laminar, transitional, and turbulent data on each geometry. All runs were performed at a 40 deg AOA.

B. Wind-Tunnel Model Design and Data Acquisition

Wind-tunnel models for each of the Mid- L/D geometries were slip-cast in silica-ceramic and coated with a thermographic phosphor

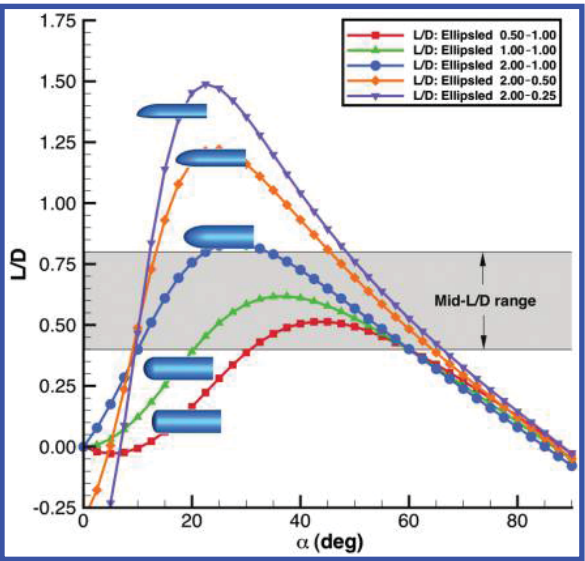


Fig. 7 Ellipsed L/D vs AOA.

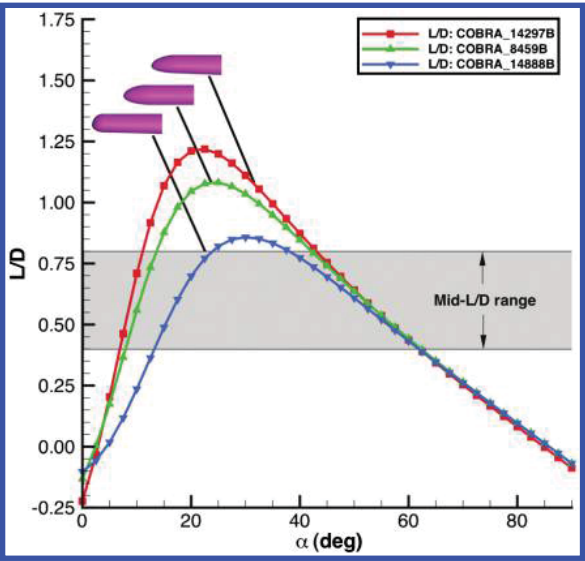


Fig. 9 COBRA L/D vs AOA.

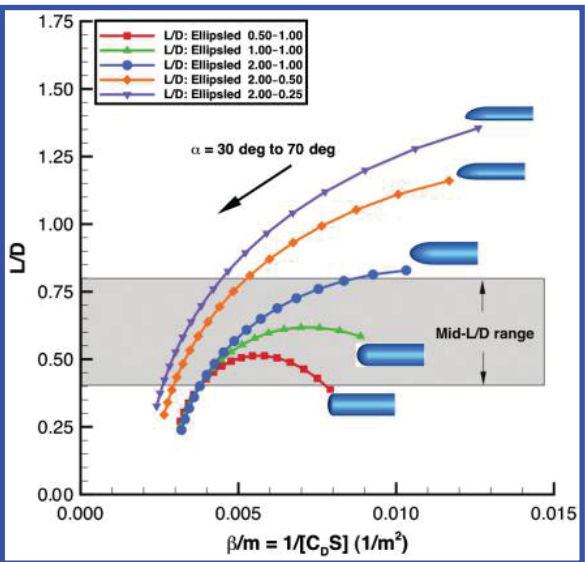


Fig. 8 Ellipsed L/D vs reduced ballistic coefficient.

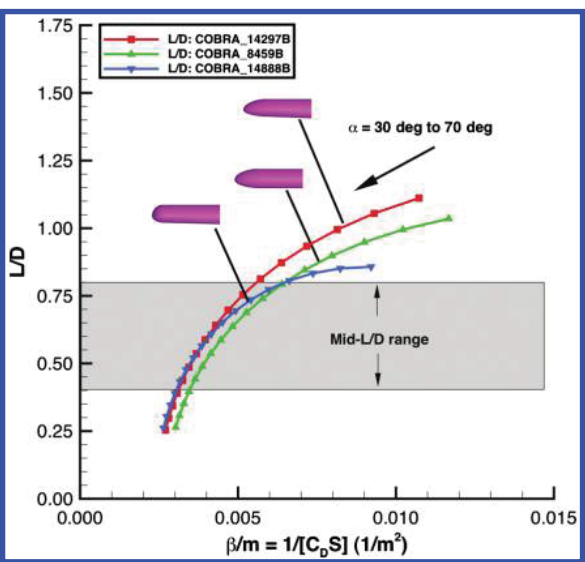
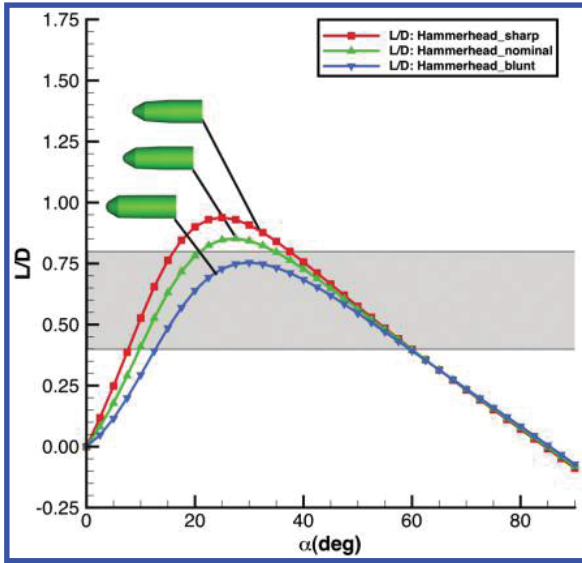
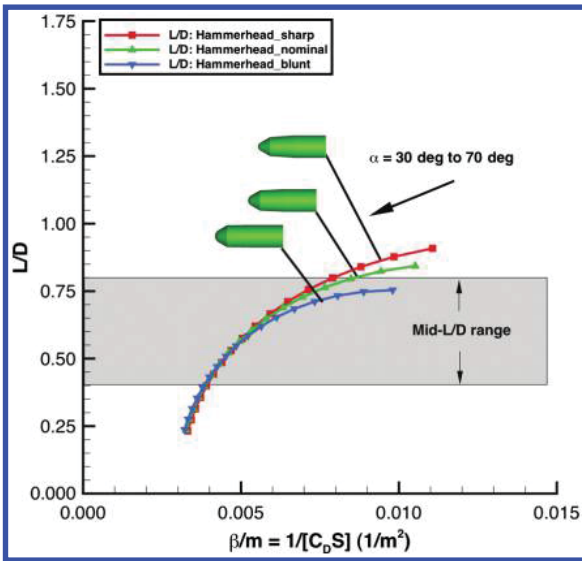


Fig. 10 COBRA L/D vs reduced ballistic coefficient.

Fig. 11 Hammerhead L/D vs AOA.Fig. 12 Hammerhead L/D vs reduced ballistic coefficient.

compound as per the process discussed in [11]. All models were 12 in. (0.3048 m) in length. Heating levels over the models were measured using the two-color, relative-intensity, global thermographic phosphor method [12,13]. In this method, heat-transfer coefficients are determined by assuming a step function in heat transfer beginning at injection of the model into the tunnel, which corresponds to a parabolic temperature-time history. The model is illuminated by ultraviolet light sources that produce temperature-dependent fluorescence of the phosphor coating, and images of the model are taken in the tunnel before and during a run using a three-

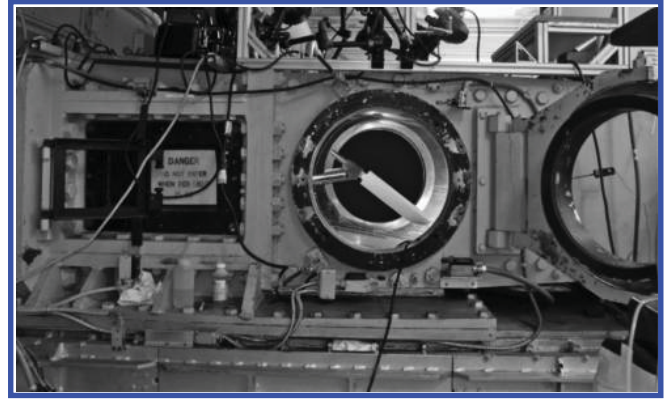


Fig. 13 NASA Langley Research Center 20 In. Mach 6 Air Tunnel.

color, charge-coupled device (CCD) camera. The Imaging for Hypersonic Experimental Aerothermodynamic Testing (IHEAT) code uses calibrations to convert the intensity data from each image pixel to temperatures and then performs the heat-transfer computations. Heat-transfer distributions in IHEAT are determined in terms of the ratio h/h_{FR} , where h_{FR} is the heat-transfer coefficient resulting from a Fay-Riddell computation [14] for a reference hemisphere. These results are then converted to a laminar heating correlation parameter defined in terms of the Stanton and Reynolds numbers, $St \times (Re_{\infty,D})^{1/2}$, where

$$St \times (Re_{\infty,D})^{1/2} = \frac{q_w}{\rho_{\infty} U_{\infty} (H_0 - H_w)} \left(\frac{\rho_{\infty} U_{\infty} D}{\mu_{\infty}} \right)^{1/2} = (h/h_{FR}) \frac{h_{FR}}{\rho_{\infty} U_{\infty}} \left(\frac{\rho_{\infty} U_{\infty} D}{\mu_{\infty}} \right)^{1/2} \quad (3)$$

The image data obtained from IHEAT are corrected for optical perspective effects and mapped to a three-dimensional (3-D) surface model for that geometry. To accomplish this mapping, perspective transformations are first performed on the 3-D surface geometry until its two-dimensional (2-D) projection matches that of the 2-D image data. The image data are then assigned transformed (x, y, z) coordinates based on interpolation between the image and surface geometry, and then the transformation is inverted to obtain an orthographic 3-D heating distribution map.

The experimental uncertainty of the measured heating levels is estimated as the root-mean-square summation of the component uncertainties due to the data acquisition method ($\pm 10\%$); flow quality and test-condition repeatability ($\pm 5\%$); and the accuracy of the 3-D mapping process ($\pm 10\%$), which results in an overall value of $\pm 15\%$. Experience with this technique indicates that these values are conservative. However, this estimate does not include multidimensional conduction effects, such as those experienced in regions of high surface curvature or imaging errors due to poor lighting or viewing angle. These effects are generally only significant at sharp nose tips (as on the flattened ellipsoids) or corners (as on the Hammerhead geometries at the junctions of the different segments) or on the sides of a model (which are tangent to the camera view angle).

Table 3 Aerodynamic performance estimates

Geometry	$L/D = 0.4$		$L/D = 0.8$	
	α , deg	β/m , $1/m^2$	α , deg	β/m , $1/m^2$
Ellipsled 0.50-1.00	60.2	0.0038	N/A	N/A
Ellipsled 1.00-1.00	60.2	0.0037	N/A	N/A
Ellipsled 2.00-1.00	60.2	0.0038	34.8	0.0084
Ellipsled 2.00-0.50	64.8	0.0029	45.8	0.0052
Ellipsled 2.00-0.25	67.0	0.0026	49.0	0.0044
COBRA 8459B	62.1	0.0035	42.5	0.0064
COBRA 14297B	62.1	0.0031	43.9	0.0054
COBRA 14888B	62.1	0.0030	38.7	0.0063
Hammerhead-blunt	60.0	0.0039	N/A	N/A
Hammerhead-nominal	60.0	0.0038	35.3	0.0084
Hammerhead-sharp	60.0	0.0037	38.2	0.0077

V. Computational Method

Flowfield predictions were performed using the Langley Aerothermodynamic Upwind Relaxation Algorithm (LAURA) code [15,16] to obtain heat-transfer rates for comparisons with the experimental data. LAURA is a 3-D, finite-volume solver that includes perfect-gas, equilibrium, and nonequilibrium chemistry models. In this study, the perfect-gas air model was used for the wind-tunnel predictions. Freestream conditions in the wind tunnel do not vary significantly from run to run, and so the nominal conditions in Table 4 were used, with the wall temperature set to a constant 300 K. The use of a constant wall temperature is acceptable because the heat-transfer coefficient varies only very slightly over the range of wall temperatures produced in this facility. Cases for turbulent flow were

Table 4 Nominal conditions for NASA Langley Research Center 20 In. Mach 6 Air Tunnel Test 6966

α , deg	Re_∞ , 1/ft	Re_∞ , 1/m	M_∞	P_∞ , Pa	T_∞ , K	ρ_∞ , kg/m ³	U_∞ , m/s	$H_0-H_{300\text{K}}$, J/kg	h_{FR} , kg/m ² /s	q_{FR} , W/cm ²
40	3.01×10^6	9.87×10^6	5.97	687	54.8	4.380×10^{-2}	882.2	1.431×10^5	2.336×10^{-1}	3.342
40	4.79×10^6	1.57×10^7	5.99	1129	56.1	7.034×10^{-2}	895.0	1.556×10^5	3.013×10^{-1}	4.688
40	6.84×10^6	2.24×10^7	6.02	1667	57.4	1.016×10^{-1}	908.0	1.686×10^5	3.685×10^{-1}	6.215
40	7.58×10^6	2.49×10^7	6.02	1879	58.1	1.132×10^{-1}	913.8	1.746×10^5	3.921×10^{-1}	6.847
40	8.33×10^6	2.73×10^7	6.03	2091	58.6	1.249×10^{-1}	918.2	1.792×10^5	4.172×10^{-1}	7.475

computed using the Cebeci–Smith algebraic turbulence model [17], which has been shown to give good comparisons to data from perfect-gas, attached-flow conditions over smooth, blunt-body geometries [18].

Structured, half-body, multiblock computational grids were generated for each configuration with 96 body-normal cells, 128 circumferential cells, and 128–160 streamwise cells (depending on configuration) and singularity-free nose blocks. For computational speed and simplicity, the aftcap and wake of the geometry was not modeled. Thus, the end of the geometry was treated as an extra-

polarization outflow boundary. Grid adaptation to the solution features was performed to align the grid outer boundary with the shock and to cluster cells near the surface to produce wall cell Reynolds numbers in the order of 1.

Because the intent of this study was to obtain experimental data, not to optimize CFD methodology, grid resolution and topology refinement have not yet been considered beyond the original grids. As will be noted in later comparisons, the use of the extrapolation outflow boundary instead of a full-wake grid, and the lack of surface grid point clustering around some topology features (e.g., the

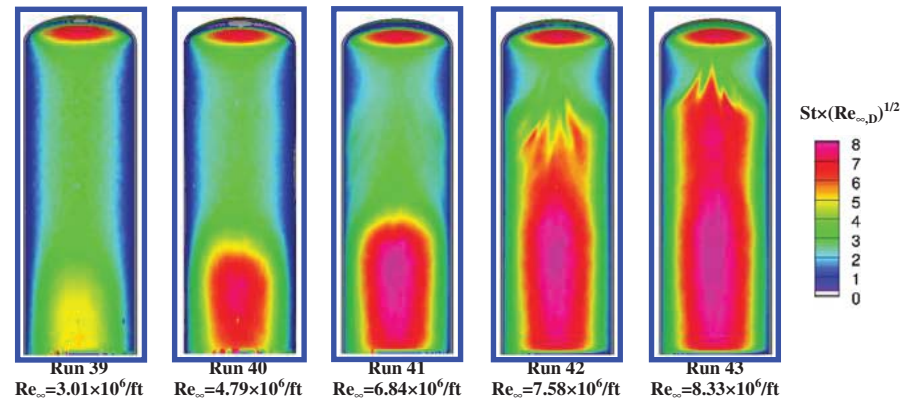


Fig. 14 Ellipsed 0.50-1.00 global heating distributions.

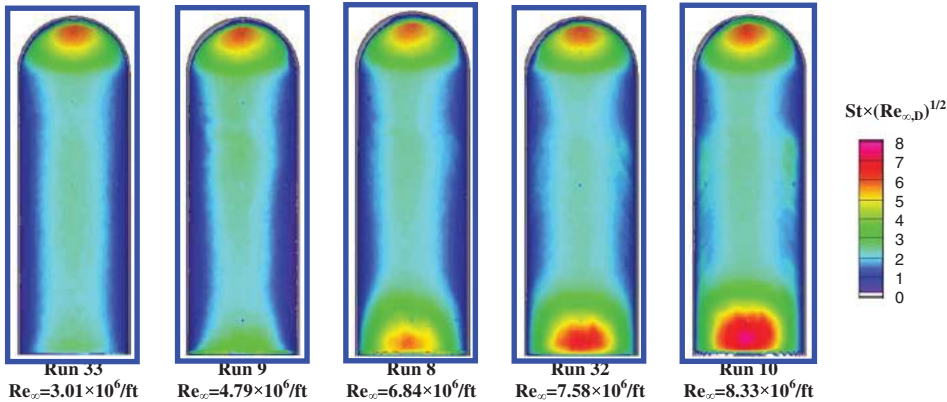


Fig. 15 Ellipsed 1.00-1.00 global heating distributions.

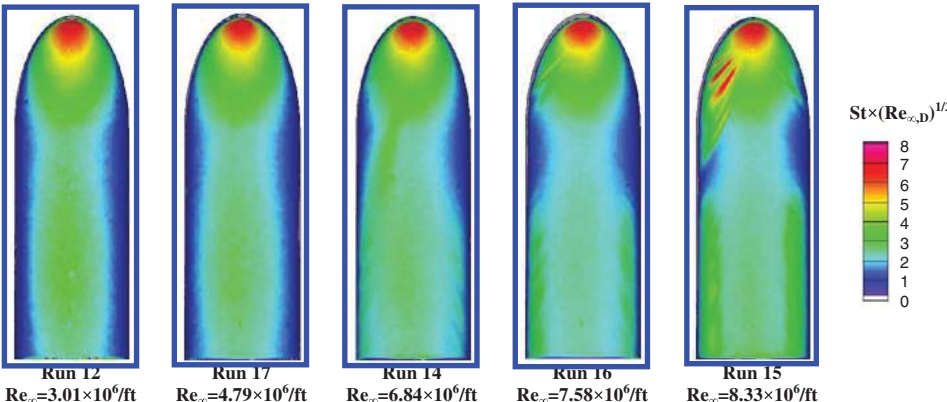


Fig. 16 Ellipsed 2.00-1.00 global heating distributions.

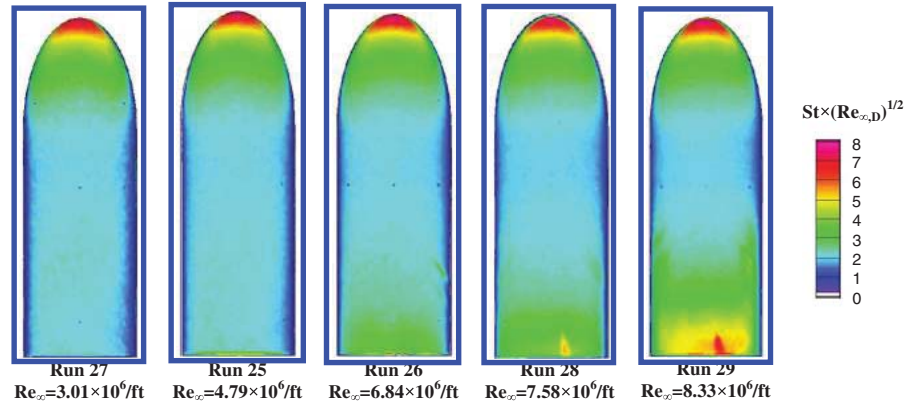


Fig. 17 Ellipsed 2.00-0.50 global heating distributions.

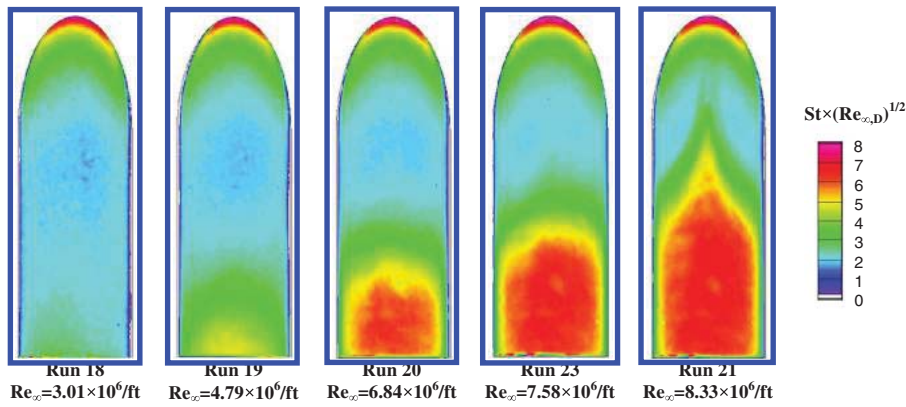


Fig. 18 Ellipsed 2.00-0.25 global heating distributions.

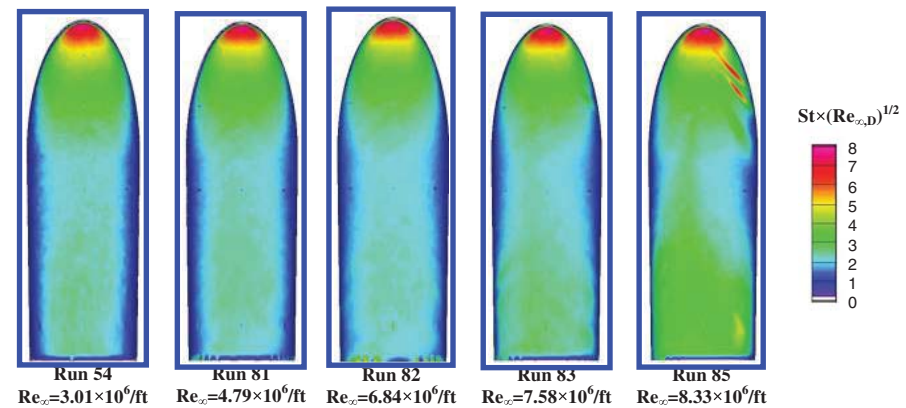


Fig. 19 COBRA 8459B global heating distributions.

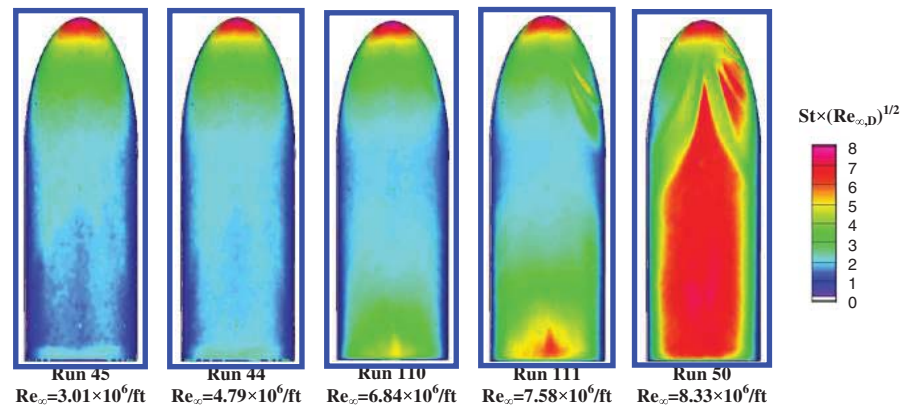


Fig. 20 COBRA 14297B global heating distributions.

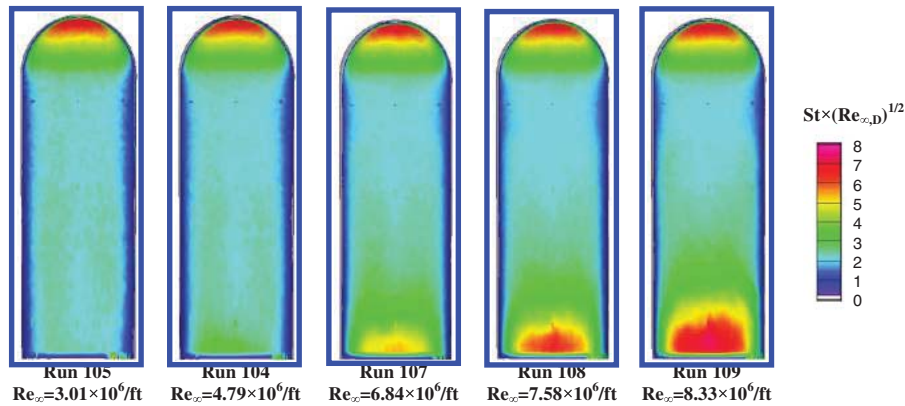


Fig. 21 COBRA 14888B global heating distributions.

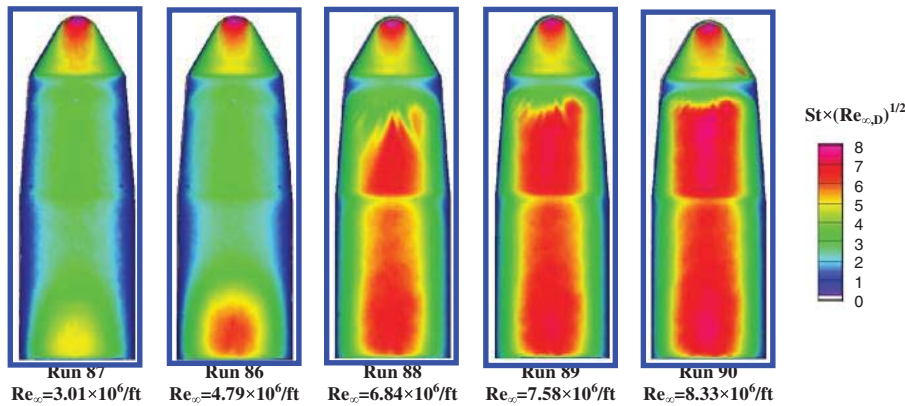


Fig. 22 Hammerhead-Sharp global heating distributions.

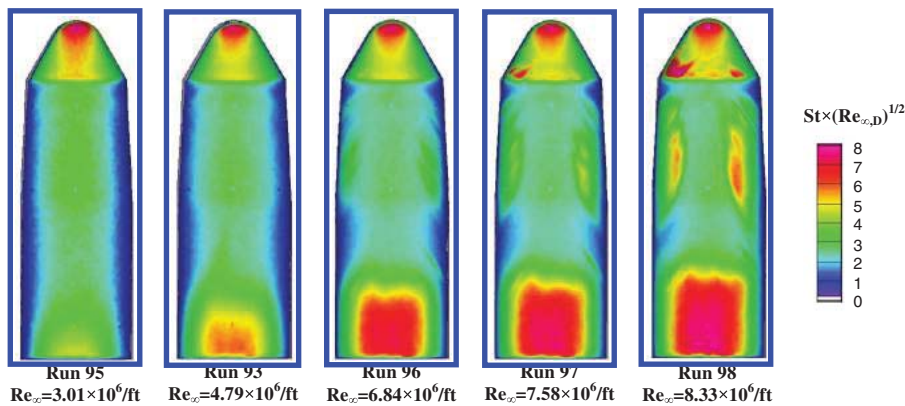


Fig. 23 Hammerhead-Nominal global heating distributions.

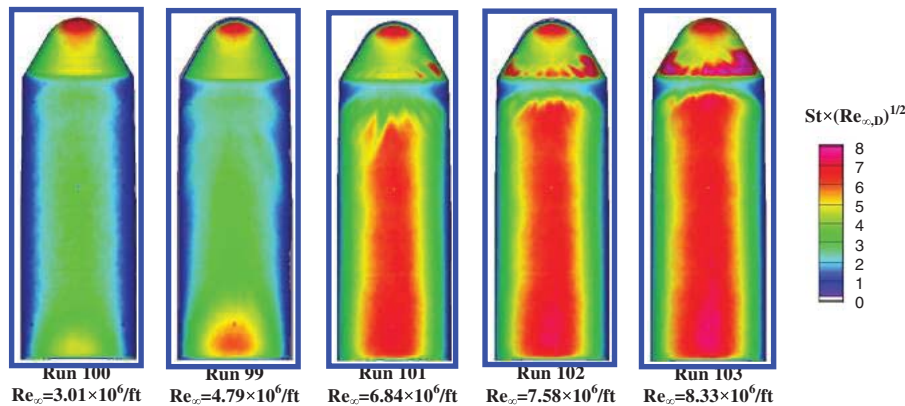


Fig. 24 Hammerhead-Blunt global heating distributions.

junctions between the Hammerhead geometry sections) likely contributed to discrepancies between predictions and data in these regions.

VI. Results and Analysis

A. Global Aeroheating Data

The 3-D mapped, global heating distributions are shown for each configuration at each of the test Reynolds numbers in Figs. 14–24 in terms of the laminar correlation parameter $St \times (Re_{\infty,D})^{1/2}$. In each

figure, the images are ordered from left to right in terms of increasing Reynolds number. Because this correlation parameter remains constant with Reynolds number for laminar flow, areas on each model where boundary-layer transition and turbulent flow occurs can be seen as changes in the heating patterns from figure to figure. In general, boundary-layer transition along the centerline was observed (at different Reynolds numbers) for all configurations except Ellipsled 2.00-1.00. In addition, outboard crossflow transition may have occurred on several of the configurations. Finally, on several of the geometries (Ellipsled 2.00-1.00, COBRA 8459B, and COBRA

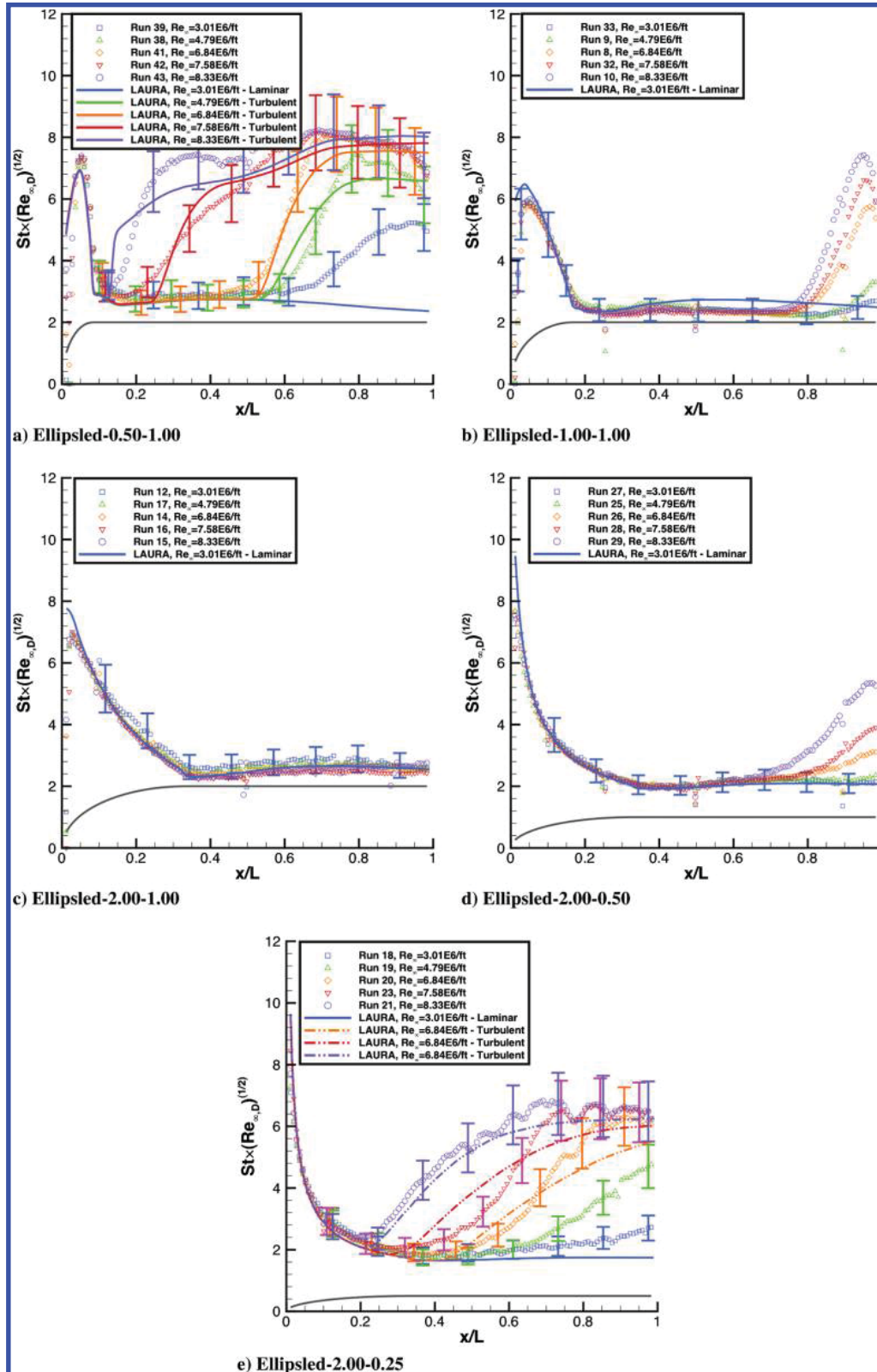


Fig. 25 Centerline heating comparisons for ellipsled configurations.

14297B), streaks near the nose may indicate transition due to slight imperfections in the surface coating or cumulative damage over the test program rather than natural “smooth-surface” transition. However, these disturbances are quickly washed outboard and do not seem to affect the centerline transition.

1. Ellipsled Configurations

Ellipsled heating distributions are shown in Figs. 14–18. Boundary-layer transition along the model centerline was observed for all ellipsled configurations except the sharpest-nosed

axisymmetric configuration Ellipsled 2.00-1.00. On the axisymmetric Ellipsled 1.00-1.00 and Ellipsled 2.00-1.00 configurations, “feathered” heating patterns of increasing strength with Reynolds number were produced outboard of the configuration oriented away from the centerline. These patterns are likely indicative of vortices from crossflow transition. No such patterns were observed on the flattened ellipsled configurations. The greatest extent of fully developed turbulent flow and highest levels of turbulent heating were produced on the axisymmetric Ellipsled 0.50-1.00 and flattened Ellipsled 2.00-0.25 configurations. Analysis of computed flowfield

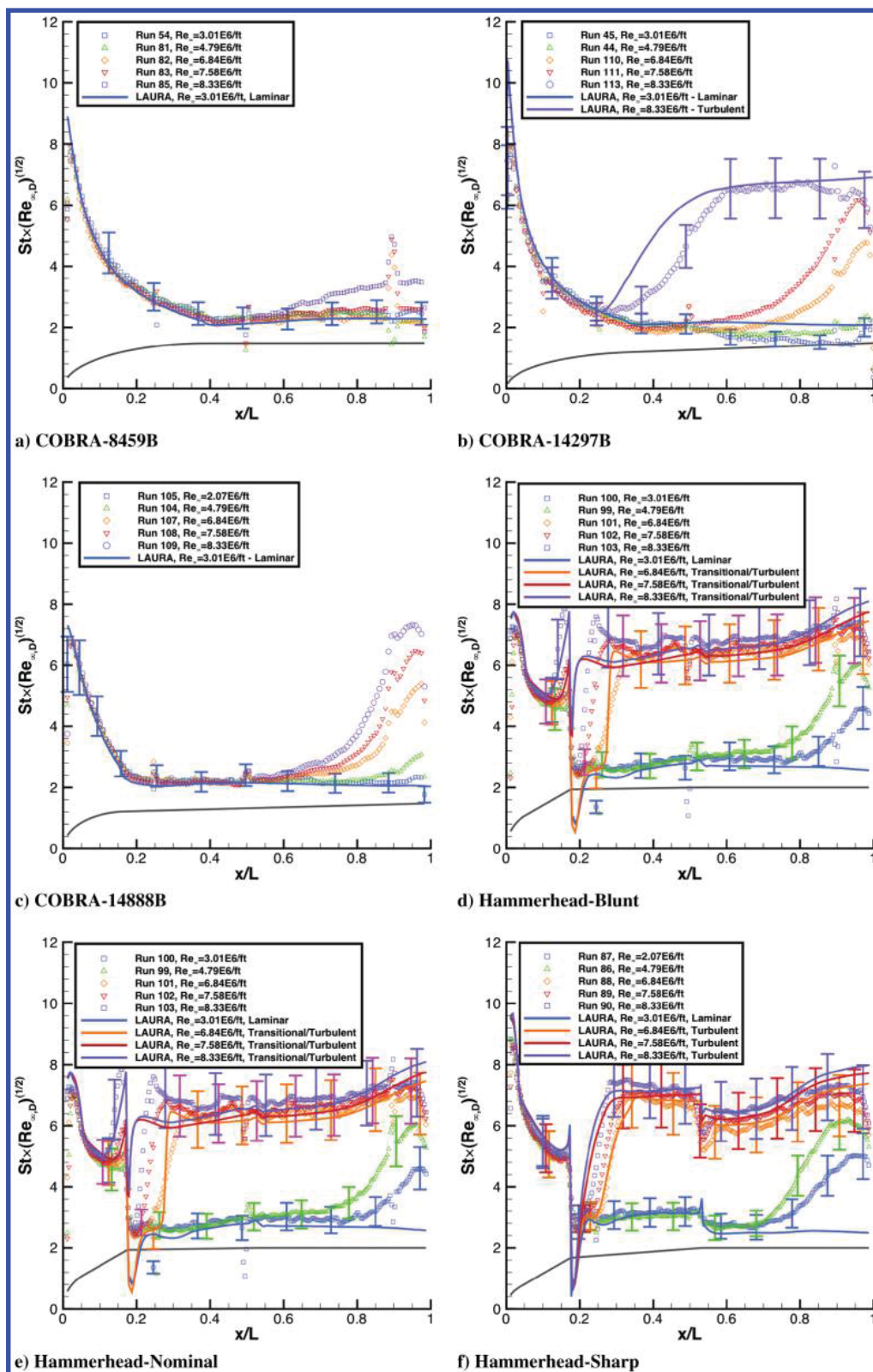


Fig. 26 Centerline heating comparisons for COBRA and Hammerhead configurations.

distributions revealed that an overexpansion and recompression shock was produced on the Ellipsled 0.50-1.00 geometry immediately downstream of the nose-cylinder junction. This flowfield feature acts to promote transition sooner than would occur via the natural, smooth-surface sensitivity to increasing Reynolds number.

2. COBRA Configurations

COBRA heating distributions are shown in Figs. 19–21. Some extent of centerline transitional and turbulent flow was observed for

all configurations at the higher Reynolds numbers. However, with the exception of the highest Reynolds number COBRA 14297B case, the extent of transitional/turbulent flow and resulting turbulent heating were lower than the ellipsled configurations. This single case may have been an anomalous early transition produced by natural roughness due to the model casting and coating process or cumulative damage to the model phosphor coating because the transition onset front near the nose appears to be more wedge-like than planar. Also, faint outboard feathering patterns near the end of the COBRA 8459B geometry may indicate crossflow transition.

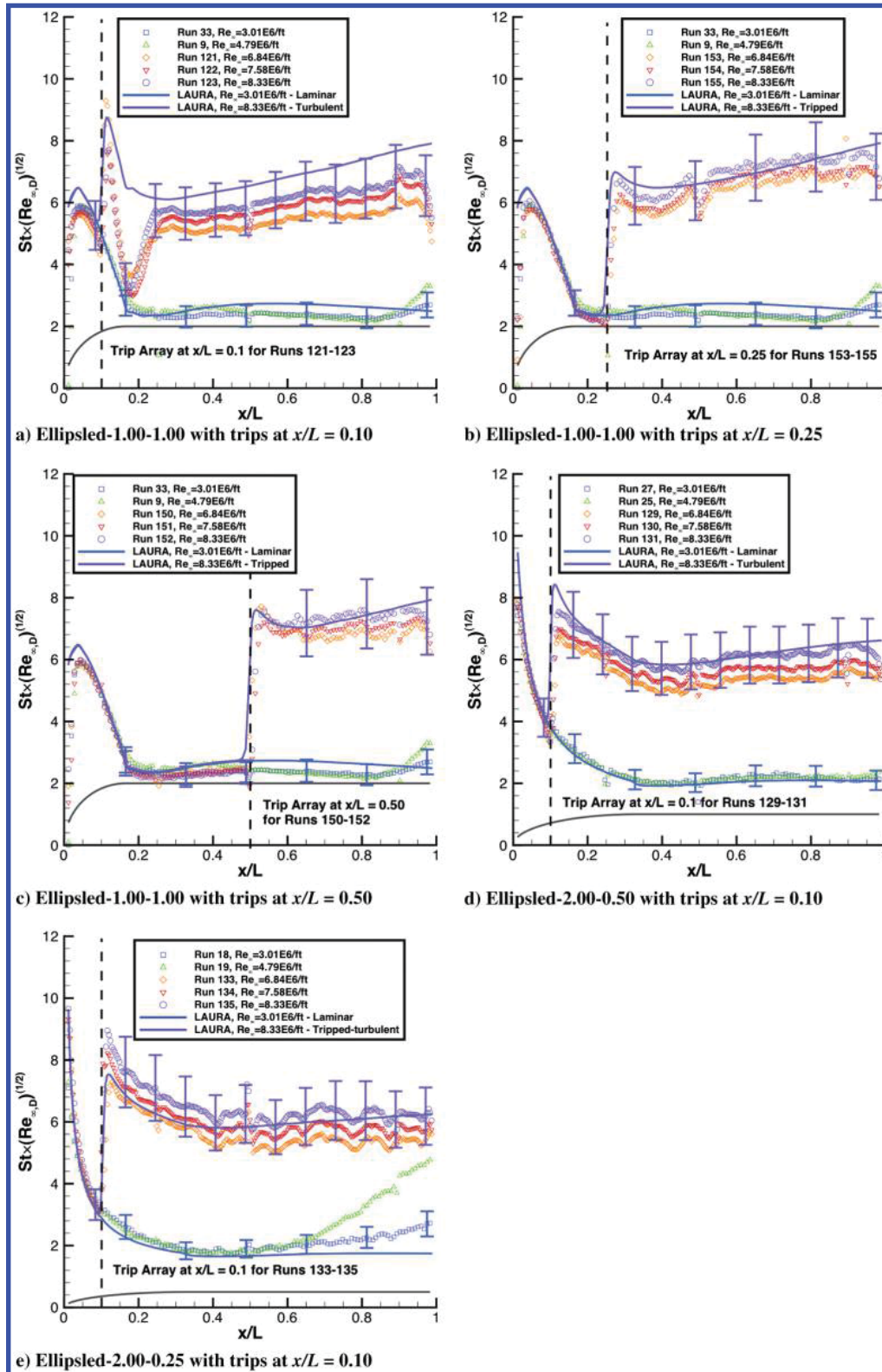


Fig. 27 Centerline heating comparisons for ellipsled configurations with trips.

Table 5 Comparison of heating levels on each geometry

Geometry	Stagnation point		Boundary-layer state	Maximum heating point on body		
	Measured $St \times (Re_{\infty,D})^{1/2}$	Location (x/L)		Measured $St \times (Re_{\infty,D})^{1/2}$	LAURA laminar $St \times (Re_{\infty,D})^{1/2}$	Heating augmentation (measured/laminar)
Ellipsled 0.50-1.00	7.35	0.69	Turbulent	8.22	2.62	3.14
Ellipsled 1.00-1.00	5.98	0.94	Transitional	7.40	2.52	2.94
Ellipsled 2.00-1.00	7.00	0.80	Laminar	2.78	2.64	1.05
Ellipsled 2.00-0.50	7.59	0.97	Transitional	5.34	2.07	2.58
Ellipsled 2.00-0.25	8.35	0.73	Turbulent	6.75	1.74	3.88
COBRA 8459B	7.78	0.95	Transitional	3.51	2.29	1.53
COBRA 14297B	7.78	0.80	Turbulent	6.74	2.11	3.19
COBRA 14888B	6.49	0.95	Transitional	7.31	2.06	3.55
Hammerhead-blunt	7.15	0.87	Turbulent	7.24	2.66	2.72
Hammerhead-nominal	7.80	0.91	Turbulent	7.53	2.61	2.89
Hammerhead-sharp	8.80	0.33	Turbulent	7.49	3.01	2.49

3. Hammerhead Configurations

Hammerhead geometry heating distributions are shown in Figs. 22–24. The Hammerhead configurations produced more complex flow patterns than the other configurations due to discontinuities in the geometric slopes between the different segments and to the proximity of the stagnation point to the junction of the nose and first cone section. For the Hammerhead-sharp and Hammerhead-blunt configurations, boundary-layer transition occurred ahead of, or almost immediately downstream of, the junction of the first and second cone sections and rapidly evolved into fully turbulent flow for all but the lowest two Reynolds numbers. In contrast, boundary-layer transition for the Hammerhead-nominal geometry did not occur until midway down the final cylindrical section. In addition, feathering patterns similar to those on the axisymmetric ellipsled were observed toward the outboard of the second cone section on the Hammerhead-nominal geometry, which was indicative of crossflow transition.

B. Measured and Predicted Heating and Transition Characteristics

Centerline comparisons between predicted and measured heating levels are presented in Figs. 25 and 26 in terms of the laminar correlation parameter $St \times (Re_{\infty,D})^{1/2}$. Laminar predictions, which are Reynolds number independent in this form, are shown for the lowest Reynolds number condition only. For Reynolds numbers where boundary-layer transition produced fully turbulent flow on a given geometry, turbulent predictions are also shown. For these turbulent computations, the transition onset location and transition length were specified based on the wind-tunnel data because the algebraic turbulent model employed does not provide a priori estimates for these properties.

Laminar data and predictions generally agreed to well within the experimental uncertainty. The only significant exception occurred on the Hammerhead geometries at the junction of the two cone sections. Predictions were much lower than measurements downstream of this location, most likely due to insufficient surface-grid clustering at this discontinuity in the geometry.

Comparisons between turbulent predictions and transitional/turbulent data were more complex. Because the algebraic turbulence model in LAURA does not predict transition onset or the length of the transition region to fully turbulent flow, these parameters were specified for the Dhawan–Narashima transition formulation [19] in LAURA to match the observed data. However, even though the transition onset location could be specified fairly accurately, the transition regime length and distribution were more difficult to match within the limits of this model. Thus, differences greater than the experimental uncertainty were produced both within and downstream of the transition region. However, the comparisons were much better for the cases where a significant length of fully turbulent flow was produced, notably on the Ellipsled 2.00-0.25, COBRA 142970B, Hammerhead-Blunt, and Hammerhead-Sharp geometries at the higher Reynolds numbers. These observations pertain only to the centerline of the geometries, where streamwise transition onset was dominant. No attempt was made to match the crossflow transition patterns that were noted on several of the configurations.

To make a better assessment of the accuracy of the Cebeci–Smith turbulence model absent the effects of transition region distribution and crossflow, an array of boundary-layer trips was employed on several of the geometries to force instantaneous streamwise transition. The arrays consisted of nine 0.05×0.05 -in.-square, 0.0035-in.-height trips spaced spanwise across the model at x/L stations of 0.10, 0.25, or 0.50 and aligned 45 deg (corner forward) toward the flow. These data and comparisons are shown in Fig. 27. With the exception of the Ellipsled 1.00-1.00 case with trips at $x/L = 0.1$, the predictions and data were in close agreement. For this anomalous case, it is possible that the placement of the trips on the curved nose section caused flow separation that disturbed the outer inviscid flow structure.

Finally, to assess the heating environments between the geometries, measured heating levels at the nose stagnation point and at the maximum heating point on the body (whether laminar, transitional, or turbulent) downstream of the nose were determined from the data. Also, the predicted laminar heating level at the maximum measured body point was taken from the predictions, and ratios of measured-to-predicted laminar heating levels were computed. These parameters are listed in Table 5. The highest stagnation-point heating was produced on the Hammerhead-Sharp configuration. The highest turbulent heating was produced on the Ellipsled 0.50-1.00 geometry, whereas the highest turbulent heating augmentation factor relative to laminar levels was produced on the Ellipsled 2.00-0.25 geometry.

VII. Conclusions

Mid- L/D entry vehicles have been proposed as an option to meet the aerodynamic performance requirements for high-mass missions to Mars and the outer planets. To provide data for mission concept development and system trade studies, the aerodynamics, convective heating, and boundary-layer transition characteristics of three families of Mid- L/D vehicles have been studied: elliptically blunted cylinders (ellipsled family); optimized parametric geometries (COBRA family); and dual-use (ascent protection and aerocapture) launch vehicle shrouds (Hammerhead family).

Aerodynamic performance estimates were produced using modified Newtonian theory. Of the 11 geometries considered, only the Ellipsled 0.50-1.00, Ellipsled 1.00-1.00, and Hammerhead-Blunt could not meet the desired requirement of L/D of 0.4 to 0.8 within angles of attack of 30 to 70 deg.

Boundary-layer transition behavior was determined from the global aeroheating measurements. All geometries experienced centerline streamwise boundary-layer transition except Ellipsled 2.00-1.00. Regions of fully developed turbulent flow were produced on the Ellipsled 0.50-1.00, Ellipsled 2.00-0.25, COBRA 14297B, and all three Hammerhead geometries. In addition to streamwise transition, feathered heating patterns indicative of crossflow transition were noted on the Ellipsled 1.00-1.00 and Ellipsled 2.00-1.00, COBRA 8459B, and Hammerhead-nominal geometries.

Comparisons between predicted laminar heating levels and measured data along the centerline agreed to well within the experimental

uncertainty for all configurations except for the Hammerhead family. On these geometries, a significant underprediction was noted around the junction of the two cone segments. This mismatch was attributed to insufficient grid resolution at this geometric discontinuity. The use of an extrapolation outflow boundary at the end of each geometry, in place of an endcap and wake-flow grid, also introduced some smaller mismatches between data and predictions at the aft end. However, both of these issues can likely be addressed through grid refinement and do not necessarily indicate any fundamental defect in the computational method.

Comparisons between transitional/turbulent data and predictions were less satisfactory. In regions of fully developed turbulent flow, agreement to within the experimental uncertainty was achieved. However, this agreement was contingent on specification of the transition onset location and transition region length in the computations based on the data rather than a priori prediction. Within the transition region, good agreement was not always obtained. In addition, the algebraic turbulence and transition model employed does not provide a mechanism for modeling the observed crossflow transition that occurred on several of the geometries.

Although the dataset is bounded by fully-turbulent predictions using the algebraic turbulence model and such predictions could be used for first order mission and design purposes, more precise and realistic predictions would require more complex computational models. The transition data from this study can be used to help develop more sophisticated correlations for streamwise transition onset for algebraic turbulence/transition models. However, to better model the crossflow transition and turbulence, it is likely that higher-fidelity turbulence modeling techniques will be required.

References

- [1] Dwyer Cianciolo, A. M., Davis, J. L., Komar, D. R., Munk, M. M., Samareh, J. A., Williams-Byrd, J. A., Zang, T. A., Powell, R. W., Shidner, J. D., Stanley, D. O., Wilhite, A. W., Kinney, D. J., McGuire, M. K., Arnold, J. O., Howard, A. R., Sostaric, R. R., Studak, J. W., Zumwalt, C. H., Llama, E. G., Casoliva, J., Ivanov, M. C., Clark, I., and Sengupta, A., "Entry, Descent and Landing Systems Analysis Study: Phase 2 Report," NASA TM-2010-216720, July 2010.
- [2] Dwyer Cianciolo, A. M., Davis, J. L., Englund, W. C., Komer, D. R., Queen, E. M., Samareh, J. A., Way, D. W., Zang, T. A., Murch, J. G., Krizan, S. A., Olds, A. D., Powell, R. W., Shidner, J. D., Kinney, D. J., McGuire, M. K., Arnold, J. O., Covington, M. A., Sostaric, R. R., Zumwalt, C. H., and Llama, E. G., "Entry, Descent and Landing Systems Analysis Study: Phase 1 Report on Exploration Feed-Forward Systems," NASA TM-2011-217055, Feb. 2010.
- [3] Dwyer Cianciolo, A. D., Davis, J. L., Shidner, J. D., and Powell, R. W., "Entry, Descent and Landing Systems Analysis: Exploration Class Simulation Overview and Results," AIAA Paper 2010-7970, Aug. 2010.
- [4] Zang, T. A., Dwyer Cianciolo, A. M., Kinney, D. J., Howard, A. R., Chen, G. T., Ivanov, M. C., Sostaric, R. R., and Westhelle, C. H., "Overview of the NASA Entry, Descent and Landing Analysis Study," AIAA Paper 2010-8649, Sept. 2010.
- [5] Lockwood, M. K., Edquist, K. T., Starr, B. R., Hollis, B. R., Hrinda, G. A., Bailey, R. W., Hall, J. L., Spilker, T. R., Noca, M. A., O'Kongo, N., Haw, R. J., Justus, C. G., Duvall, A. L., Keller, V. W., Masciarelli, J. P., Hoffman, D. A., Rea, J. R., Westhelle, C. H., Graves, C. A., Takashima, N., Olejniczak, J., Chen, Y. K., Wright, M. J., Laub, B., Prabhu, D., Dyke, R. E., and Prabhu, R. K., "Aerocapture System Analysis for a Neptune Mission," NASA TM-2006-214300, April 2006.
- [6] Drake, B. G., "Reference Mission Version 3.0 Addendum to the Human Exploration of Mars: The Reference Mission of the NASA Mars Exploration Study Team," NASA SP-1998-6107/ADD, June 1998.
- [7] Garcia, J. A., Brown, J. L., Kinney, D. J., Bowles, J. V., Huynh, L. C., Jiang, X. J., Lau, E., and Dupzyk, I. C., "Co-Optimization of Mid Lift to Drag Vehicle Concepts for Mars Atmospheric Entry," AIAA Paper 2010-5052, July 2010.
- [8] Drake, B. G., "Human Exploration of Mars Design Reference Architecture 5.0," NASA SP-2009-566, July 2009.
- [9] Borowski, S. K., McCurdy, D. R., and Packard, T. W., "7-Launch NTR Space Transportation System for NASA's Mars Design Reference Architecture (DRA) 5.0," AIAA Paper 2009-5308, Aug. 2009.
- [10] Micol, J. R., "Langley Aerothermodynamic Facilities Complex: Enhancements and Testing Capabilities," AIAA Paper 98-0147, Jan. 1998.
- [11] Buck, G. M., "Rapid Model Fabrication and Testing for Aerospace Vehicles," AIAA Paper 2000-0826, Jan. 2000.
- [12] Buck, G. M., "Surface Temperature/Heat Transfer Measurement Using a Quantitative Phosphor Thermography System," AIAA Paper 91-0064, Jan. 1991.
- [13] Merski, N. R., "Global Aeroheating Wind-Tunnel Measurements Using Improved Two-Color Phosphor Thermography Methods," *Journal of Spacecraft and Rockets*, Vol. 36, No. 2, 1999, pp. 160–170. doi:10.2514/2.3446
- [14] Fay, J. A., and Riddell, F. R., "Theory of Stagnation Point Heat Transfer in Dissociated Air," *Journal of the Aeronautical Sciences*, Vol. 25, No. 2, 1958, pp. 73–85.
- [15] Gnoffo, P. A., "An Upwind-Biased, Point-Implicit Algorithm for Viscous, Compressible Perfect-Gas Flows," NASA TP-2953, Feb. 1990.
- [16] Mazaheri, A., Gnoffo, P. A., Johnston, C. O., and Kleb, B., "LAURA User's Manual: 5.4-54166," NASA TM-2011-217092, May 2011.
- [17] Cheatwood, F. M., and Thompson, R. A., "The Addition of Algebraic Turbulence Modeling to Program LAURA," NASA TM-107758, April 1993.
- [18] Hollis, B. R., "Blunt-Body Entry Vehicle Aerothermodynamics: Transition and Turbulence on the CEV and MSL Configurations," AIAA Paper 2010-4984, July 2010.
- [19] Dhawan, S., and Narashima, R., "Some Properties of Boundary Layer Flow from Laminar to Turbulent Motion," *Journal of Fluid Mechanics*, Vol. 1, No. 4, 1958, pp. 418–436.

G. Palmer
Associate Editor